Nanoscale

Branched Aramid Nanofiber-Polyaniline Electrodes for Structural Energy Storage

Journal:	*Nanoscale*
Manuscript ID	NR-ART-06-2020-004573.R1
Article Type:	Paper
Date Submitted by the Author:	29-Jul-2020
Complete List of Authors:	Flouda, Paraskevi; Texas A and M University College Station Quinn, Alexander; MIT, Patel, Anish; Texas A and M University College Station, Chemical Engineering Loufakis, Dimitrios; Texas A and M University College Station Lagoudas, Dimitris C.; Texas A and M University College Station Lutkenhaus, Jodie; Texas A&M University,

ARTICLE

Branched Aramid Nanofiber-Polyaniline Electrodes for Structural Energy Storage

Received 00th January 20xx,
Accepted 00th January 20xx

DOI: 10.1039/x0xx00000x

Paraskevi Flouda,[a] Alexander H. Quinn,[b] Anish G. Patel,[b] Dimitrios Loufakis,[a] Dimitris C. Lagoudas,[a,c] and Jodie L. Lutkenhaus[a,b,*]

Strong electrodes with good energy storage capabilities are necessary to accommodate the current needs for structural and flexible electronics. To this end, conjugated polymers such as polyaniline (PANI) have attracted much attention due to their exceptional energy storage performance. However, PANI is typically brittle and requires the use of substrates for structural support. Here, we report a strategy for developing free-standing structural supercapacitor and battery electrodes based on PANI. More specifically, aniline is polymerized in the presence of branched aramid nanofibers (BANFs) and single walled carbon nanotubes (SWCNTs). This results in a network morphology created that allows for efficient load transfer and electron transport, leading to electrodes with capacity values up to 128 ± 5 mAh/g (*vs.* a theoretical capacity of 147 mAh/g), Young's modulus of 4 ± 0.5 GPa, and tensile strength of 40 ± 4 MPa. Furthermore, the charge storage mechanism is investigated, in which both Faradaic and non-Faradaic contributions are observed. This work demonstrates an efficient strategy for designing structural electrodes based on conjugated polymers.

Introduction

Mechanically strong energy storage devices, such as supercapacitors and batteries, are in high demand in the developing markets of flexible, wearable, and structural electronics.[1-3] Polyaniline (PANI) is a promising electrode material for electrochemical energy storage due to its tuneable morphology and pseudocapacitive response.[4] However, PANI has poor mechanical properties and, as a result, is unfit to support mechanical loads in devices.[5] Here, we present a strategy for mechanically strong PANI-based electrodes for structural supercapacitors and Li-ion batteries by taking advantage of composite structures.

PANI, a p-type conjugated polymer, has been extensively studied as an electrode material due to its high electrical conductivity (2-5 S/cm when in emeraldine salt form) and high theoretical capacity (147 mAh/g, assuming one electron exchange for every two repeat units), as well as its low cost and ease of synthesis.[6-11] PANI is redox active and stores charge though a reversible doping-dedoping mechanism, which depends strongly on the anion in the electrolyte.[6-8, 12] As a result, PANI and its composite derivatives have been explored as pseudocapacitive electrode materials in supercapacitors and Li-ion batteries.[13] As a supercapacitor electrode, PANI/reduced graphene oxide (rGO) exhibited an electrical conductivity of 5.5 S/cm and specific capacitance of 210 F/g.[14] Carbon nanotube (CNT)/PANI electrodes demonstrated electrical conductivities up to 150 S/cm and specific capacitances up to 424 F/g.[15] Additionally, PANI has been studied as a cathode material for Li-ion batteries. Most battery-based studies focus on PANI-coated on conductive substrates using layer-by-layer (LbL) methods.[8, 11, 16, 17] PANI/rGO LbL electrodes exhibited electrical conductivities of 1.84 S/cm and capacities of 188 mAh/g, whereas PANI/MXene LbL electrodes showed capacities up to 145 mAh/g.[11, 18] Although there are limited number reports on free-standing PANI films,[19-21] there are no examples of PANI-based electrodes for structural batteries.

Despite the extensive studies on the electrical and electrochemical performance of PANI, there are only a handful of studies on its mechanical performance.[22] Single PANI fibers exhibited electrical conductivities of 600 S/cm, Young's moduli of 2 GPa, and tensile strength of 105 MPa after doping.[23] Pure PANI films are generally plagued by brittleness and low ductility.[24] However, studies on PANI composite films show promise. For instance, PANI/cellulose membranes exhibited a Young's modulus of 5.6 GPa and tensile strength of 95.7 MPa, but the electrical conductivities were as low as 0.05 S/cm.[25]

We hypothesized that the mechanical performance of PANI composites may be improved by the addition of strong polymers such as branched aramid nanofibers (BANFs). This hypothesis is motivated by our prior work, in which BANFs dramatically improved the mechanical properties of rGO-based electrodes.[3, 26-32] BANFs are nanoscale Kevlar fibers derived by the dissolution of bulk Kevlar fiber in dimethyl sulfoxide and potassium hydroxide.[33-36] PANI/ANF composites (using un-branched ANFs) have been previously explored for sensors, EMI

[a] *Department of Materials Science and Engineering, Texas A&M University, College Station, TX 77843, USA.*
[b] *Artie McFerrin Department of Chemical Engineering Texas A&M University, College Station, TX 77843, USA.*
[c] *Department of Aerospace Engineering, Texas A&M University, College Station, TX 77843, USA.*
† Electronic Supplementary Information (ESI) available: Experimental details and supplementary figures. See DOI: 10.1039/x0xx00000x

shielding, and flexible supercapacitor electrodes.[37-40] PANI filtered through a premade matrix of ANF exhibited high electrical conductivities of 20-300 S/cm and good mechanical properties with a Young's modulus of ~5 GPa and a tensile strength of 179 MPa.[37] Similarly, PANI/ANF core-shell composites demonstrated electrical conductivities of $0.05 \cdot 10^{-2}$ S/cm, Young's moduli of 1.3 GPa, and tensile strengths of 50 MPa.[39] PANI grown directly on ANF premade films showed a Young's modulus of 4 GPa, tensile strength of 233 MPa, and a specific capacitance of 138 F/g in a two-electrode symmetric solid state cell.[40] We expect branched ANFs to lead to further improvements in mechanical performance as it has also been demonstrated in our prior work on rGO/ANF and rGO/BANF structural electrodes due to the higher surface area available for hydrogen bonding and π-π stacking interactions.[27, 28, 41] Despite progressive studies on the mechanical properties of PANI/ANF composites, the effects of BANF on the mechanical and energy storage performance of PANI in both supercapacitors and batteries are still unexplored.

Here, aniline was polymerized in the presence of BANFs and single walled carbon nanotubes (SWCNTs) to create strong and conductive networks for structural capacitors and batteries. Free-standing thin film electrodes of high BANF content (50 - 80 wt%) were fabricated using vacuum filtration of the three components. PANI acted as the redox-active component for energy storage, and PANI's combination with CNTs leads to more accessible redox sites.[42] Furthermore, CNTs were chosen due to their high electrical conductivity (~ 10^3 S/cm) and high surface area (120 – 500 m^2/g),[43-45] which we hypothesized might further enhance the electrochemical performance of the structural electrodes. As it has been demonstrated before in rGO/Co_9S_8 and rGO/MnO_2/CNTs electrodes for Li-ion batteries and supercapacitors, the combination of redox active materials with high surface area conductive materials leads to improved energy storage performance.[46, 47] The morphology and composition were investigated using scanning electron microscopy (SEM), transmission electron microscopy (TEM), energy dispersive spectroscopy (EDS), and Raman spectroscopy. The mechanical properties were assessed using uniaxial tensile testing. Finally, the PANI/BANF/CNT electrodes were investigated in symmetric supercapacitors and in Li-ion batteries. An electrochemical analysis of the charge-storage mechanism was also applied. Altogether, this work demonstrates the first design of structural electrodes based on PANI for both supercapacitors and Li-ion batteries.

Experimental

Aniline, ammonium persulfate (APS), hydrochloric acid (HCl), dimethyl sulfoxide (DMSO), 1 M lithium hexafluorophosphate ($LiPF_6$) in ethylene carbonate:dimethylene cabonate:diethylene carbonate (EC:DMC:DEC) (1:1:1 v/v), Li metal foil, branched polyethyleneimine (b-PEI, MW = 25,000 g/mol, MN = 10,000 g/mol), sodium nitrate ($NaNO_3$), hydrogen peroxide (H_2O_2), potassium permanganate ($KMnO_4$), and sulfuric acid (H_2SO_4) were purchased from Sigma-Aldrich. Kevlar®69 thread was purchased from Thread Exchange. Carbon paper was purchased from Alfa Aesar. Celgard 3501 was provided by Celgard. Spectra/Por dialysis tubes of 12-14 kD molecular weight cut-off were purchased from VWR. Single-walled carbon nanotubes (SWCNTs, diameter: 1.8 nm), carboxylated multi-walled carbon nanotubes (MWCNTs-COOH), and graphite (SP-1) were purchased from Tuball, CheapTubes, and Bay Carbon, respectively.

Chopped Kevlar fiber (0.5 g) was mixed with KOH (0.5 g) in DMSO (50 ml).[33] The mixture was stirred for seven days to obtain a dark red viscous dispersion of BANF/DMSO (10 mg/ml). Dialysis of a BANF/DMSO (1 mg/ml) mixture was performed for 3 days to exchange water for DMSO.

BANF/water dispersions (1 mg/ml) were mixed with SWCNTs/water (1 mg/ml) dispersions at desired ratios. The mixture was ultrasonicated for 5 min and stirred for 1 h to form homogeneous BANF/CNT dispersions. Aniline monomer (30 mg) was mixed with the BANF/CNT dispersion (20 ml of 1 mg/ml) for 1 h under nitrogen. APS (0.69 g) was added in 1M HCl (20 ml) and stirred for 1 h under nitrogen. The two dispersions were rapidly mixed together under nitrogen for 24h.[39] Thin films were fabricated through vacuum filtration using a Nylon filter paper (pore size: 0.2 µm and diameter: 47 mm). The total mass of the composites was kept constant at ~20 mg. Finally, the films were washed with a 1M HCl solution and dried under vacuum at 60 °C for 3 days.

Raman spectra were collected using a Horiba JobinYvon spectrometer with excitation at 514 nm. FT-IR/ATR was conducted using IR Prestige 21 system, equipped with a diamond ATR lens (Shimadzu). Scanning electron microscopy images were obtained using a JEOL, SM-7500F SEM with an Oxford EDS system. Electrical conductivity measurements were obtained using a four-point probe.

Tensile testing was conducted using a DMA Q8OO (TA Instruments) with a strain rate of 0.1 %/min and preload force of 0.02 Nt. All measurements were conducted at room temperature and humidity (~23 °C and 30-35 %).

Two-electrode symmetric coin cells were used for supercapacitor testing. Electrodes of mass loadings of 1.5 - 2 mg/cm^2 (per total electrode mass) were used. 6M KOH was used as the aqueous electrolyte, Celgard 3501 as the separator, and carbon paper as the current collector. Two stainless steel spacers and a spring were used. The electrochemical testing was conducted using a potentiostat (Gamry Interface 1000, Gamry Instruments). Cyclic voltammetry tests were conducted at a potential window of -0.2-0.8 V and varying scan rates (1-100 mV/s). Galvanostatic cycling experiments were conducted at the same potential window under different specific currents (0.2-2 A/g). The specific capacitance was calculated as described previously.[3] Half-cell battery testing was conducted using a two-electrode setup (Tomcell). The electrochemical test was conducted using a Solatron (Electrochemical Interface 1287). The working electrodes (same mass ladings as with the supercapacitor electrodes) were further dried under vacuum overnight at 60 °C. Li metal foil was used as the counter/reference electrode and 1M $LiPF_6$ in 1:1:1 (v/v) EC:DEC:DMC was used as the electrolyte. Celgard 3501 was used as the separator. Cyclic voltammetry tests were performed at various scan rates (1 – 100) mV/s and galvanostatic cycling

tests at varying specific currents (50 – 1000 mA/g). All electrodes were preconditioned with 50 cycles of cyclic voltammetry at 20 mV/s. Electrochemical impedance spectroscopy (EIS) was performed using a potentiostat (Gamry Interface 1000, Gamry Instruments) at 3.3 V *vs.* Li/Li^+ with a 5 mV amplitude and frequency range of 1 MHz - 100 mHz.

Results and discussion

Fabricating PANI-containing free-standing electrodes is challenging due to PANI's poor mechanical properties and inability to disperse in various solvents.[8, 22] Our different attempts to fabricate PANI-based electrodes are summarized in Table S1, ESI†. Initially, PANI/water dispersions were directly vacuum filtrated, however, brittle films that cracked upon drying were formed. To improve the mechanical performance of the films, BANFs (10 wt%) were added to the PANI dispersions followed by vacuum filtration. However, the poor stability of the PANI/BANF dispersion led to inhomogeneous films that also cracked while drying.[8] To avoid this, a two-layer vacuum filtration (1st layer BANF and 2nd layer PANI) was performed, but the obtained electrodes exhibited inferior electrochemical performance resulting from poor electrical percolation. Further attempts were made using PANI:poly(2-acrylamido-2-methyl-1-propanesulfonic acid) (PAAMPSA) as PANI:PAAMPSA complexes form more stable dispersions.[8] Various third components were also added to alleviate the brittleness, such as branched polyethyleneimine (b-PEI), carboxyl functionalized multi-walled carbon nanotubes (MWCNTs-COOH), and graphene oxide (GO). Finally, polymerization of aniline in the presence of BANF and single walled carbon nanotubes (SWCNTs) was selected as it led to homogeneous electrodes with desirable mechanical and electrical properties.

Preparation of the electrode first proceeded by slow dialysis of the BANF/DMSO mixture to exchange water for DMSO. Then, desired amounts of pristine SWCNTs were added to the BANF/water dispersion followed by ultrasonication. Aniline was polymerized in the presence of BANFs (diameter = 15-30 nm)[28] and SWCNTs (diameter = 1.8 nm) to obtain a network morphology. Fig. 1a-1c shows SEM and TEM images of PANI/BANF/CNT bundles forming continuous networks. The shadow in Fig. 1c is indicative of PANI, as observed before in similar structures.[39, 48] However, we cannot distinguish BANFs from SWCNTs. Additionally, PANI formation was confirmed using EDS and Raman spectroscopy as discussed in more detail below.

Mechanically strong electrodes were fabricated using vacuum-assisted filtration, as shown in Fig. 1d and 1e. The final PANI compositions of the composite electrodes were estimated using the gravimetric method, as shown in Table S2, ESI†. The electrodes were composed of ~15 wt% PANI, whereas the remaining ~85 wt% was divided among BANFs and SWCNTs at desired ratios. Unless otherwise specified, "PANI/BANF/CNT" corresponds to an electrode having a composition of 15 wt% PANI, 73 wt% BANF, and 12 wt% SWCNT.

SWCNT and PANI addition were verified using EDS, Raman spectroscopy, and FT-IR spectroscopy on BANF, BANF/CNT, and PANI/BANF/CNT composites, as shown in Fig. 2a-c, Fig. S1, Table S3 and S4, ESI†. EDS mapping of the N element of the composite surface (Fig. 2a-c) qualitatively showed a decrease in N content upon addition of SWCNT (BANF/CNT *vs.* BANF). Furthermore, PANI addition (PANI/BANF/CNT) caused an increase in N, indicating the successful aniline polymerization in the presence of BANF/CNT.

Raman spectra are shown in Fig. S1a and Table S3, ESI†. More specifically, BANFs exhibited peaks due to C=C stretching

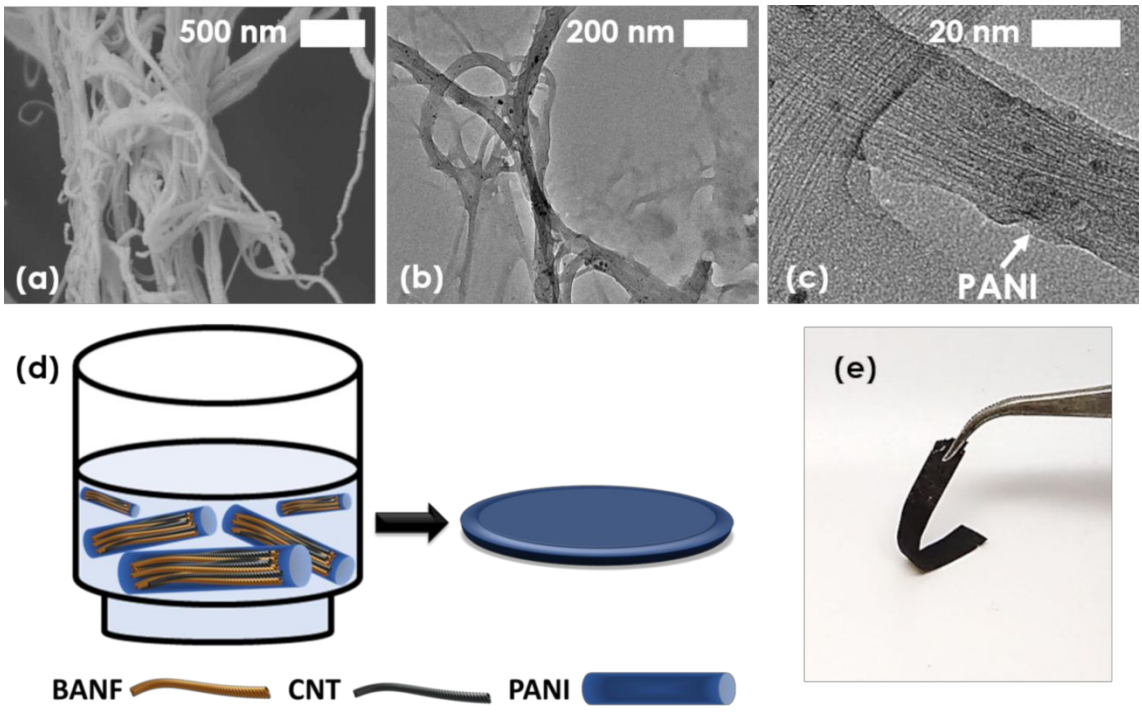

Fig. 1 SEM (a) and TEM (b and c) images of PANI/BANF/CNT bundles. (d) Schematic representation for the vacuum filtration of the PANI/BANF/CNT bundles and (e) digital image of the composite PANI/BANF/CNT electrode.

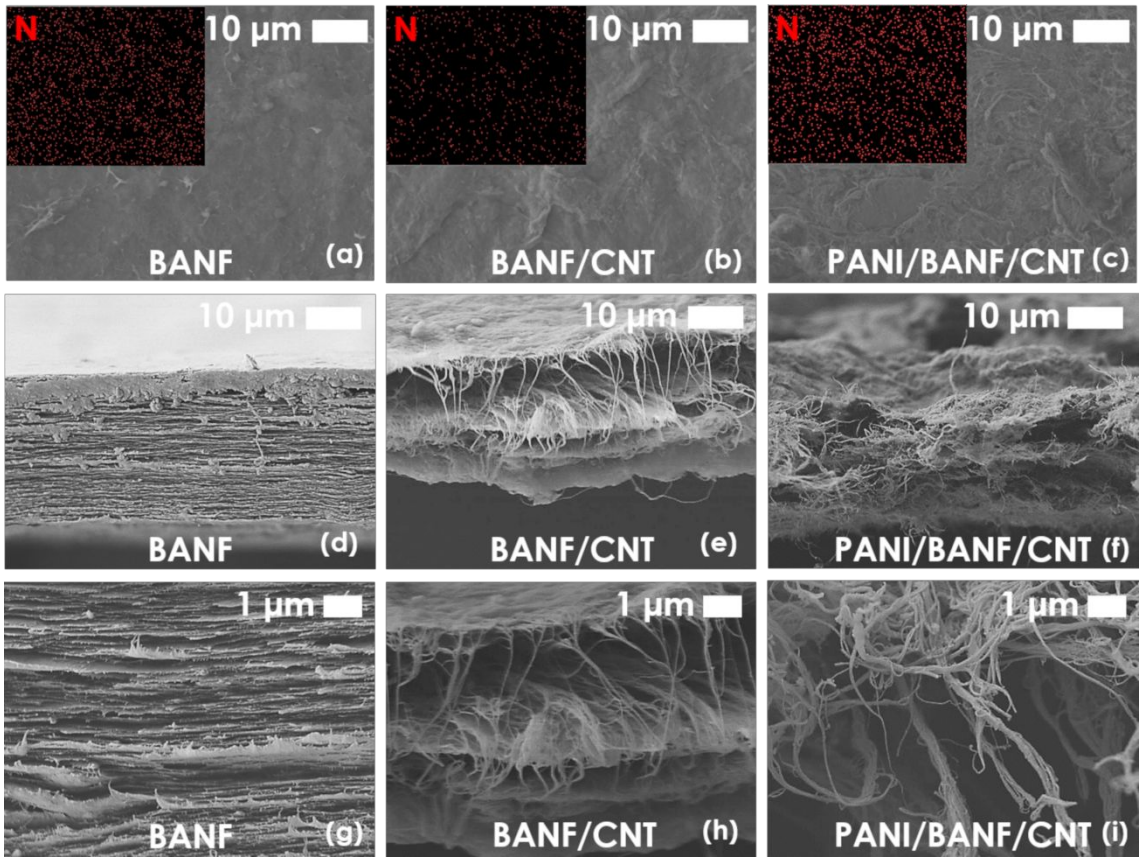

Fig. 2 (a-c) SEM images and EDS mapping of the N element for BANF, BANF/CNT, and PANI/BANF/CNT surfaces. Cross-sectional SEM images for BANF (d, g), BANF/CNT (e, h), and PANI/BANF/CNT (f, i) at low (d-f) and high (g-i).

(1176, 1267, 1508, and 1608 cm^{-1}), C-H in-plane bending (1321 cm^{-1}), N-H bending/C-N stretching (1564 cm^{-1}), and C=O stretching (1650 cm^{-1}) modes.[26, 49] BANF/CNT exhibited the G-band at 1588 cm^{-1} resulting from the SWCNT's sp^2-hybrized carbon atoms.[50] PANI/BANF/CNT spectra showed two broad peaks at 1260 – 1450 cm^{-1} and 1490 – 1610 cm^{-1} resulting from the additional contribution of the PANI C-N stretching (1331 cm^{-1}) and C=N stretching (1496 cm^{-1}) modes.[7, 18, 51] These observations demonstrate that SWCNTs and PANI were successfully incorporated in the BANF composites.

The addition of SWCNTs and PANI was also confirmed using FT-IR spectroscopy, as shown in Fig. S1b and Table S4, ESI†. BANF exhibited peaks due to C-H in-plane deformation (1173 cm^{-1}), C-N stretching of secondary aromatic amines (1318 cm^{-1}), C-H bending (1490 cm^{-1}), C=C stretching (1515 cm^{-1}), N-H deformation and C-N stretching coupled modes (1545 cm^{-1}), C=O stretching (1645 cm^{-1}), and N-H stretching (3300 cm^{-1}).[34] Upon addition of SWCNTs (BANF/CNT) the intensity of the C=C peak increased as a result of the additional SWCNT sp^2-hybrized carbon atoms.[52] Furthermore, PANI/BANF/CNT exhibited peaks due to C-N stretching of secondary aromatic amines (1173 cm^{-1}) and N-B-N stretching (1490 cm^{-1}), where B represents benzenoid and Q quinoid moieties in PANI.[37] The PANI peaks are difficult to distinguish in the FT-IR spectra due to the low PANI composition (~15 wt%) and the location of the peaks.

The morphology of the composites with different compositions was investigated using SEM, as shown in Fig. 2d - 2i and Fig. S2, ESI†. BANF films showed a highly layered structure and thicknesses varying from 22-30 μm. The layered structure was maintained upon addition of SWCNT (BANF/CNT) and PANI (PANI/CNT) as shown in Fig. 2e and Fig. S2, ESI†, respectively. In both cases the SWCNTs were visible from the cross-sectional SEM images; however, the addition of PANI led to a less distinguishable layered structure. BANF/CNT, PANI/CNT, and PANI/BANF/CNT composites displayed thicknesses of 5-15 μm.

Tensile tests were conducted to evaluate the mechanical properties of the composites, as shown in Fig. 3a-c and Table S5, ESI†. BANF films exhibited the highest tensile strength (138 ± 5.3 MPa), stain to failure (8.5 ± 0.2 %), and toughness (7100 ± 175 kJ/m^3) with an intermediate Young's modulus of 3.0 ± 0.1 GPa. The mechanical performance of the BANF films was similar to other ANF-based films reported in the literature.[53-58] Addition of 14 wt% SWCNTs (BANF/CNT) led to a deteriorated mechanical performance due to the dilution of the strong and stiff BANFs. More specifically, tensile strength decreased by 54 % (to 64 ± 6 MPa), Young's modulus by 17 % (to 2.5 ± 0.2 GPa), ultimate strain by 36 % (to 5.4 ± 0.9 %), and toughness by 73 % (to 1900 ± 350 kJ/m^3). PANI/BANF and PANI/BANF/CNT electrodes exhibited lower tensile strength, ultimate strain, and toughness but higher Young's modulus as compared to BANF/CNT. Specifically, PANI/BANF (15 wt% PANI) possessed the highest Young's modulus (5.4 ± 0.6 GPa) with a tensile strength of 58 ± 1.4 MPa, an ultimate tensile strain of 1.9 ± 0.4

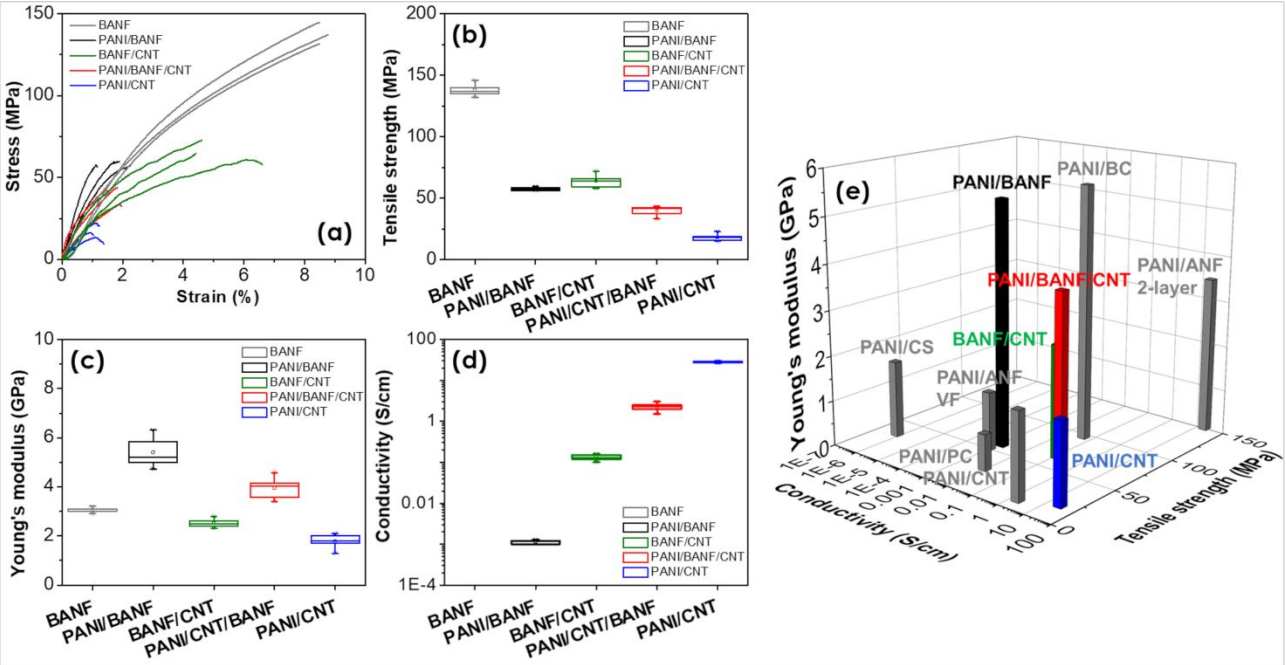

Fig. 3 (a) Representative stress-stain curves for BANF, BANF/CNT, PANI/BANF, PANI/BANF/CNT, and PANI/CNT. Box plots for (b) tensile strength, (c) Young's modulus, and (d) electrical conductivity. (e) Ashby plot of Young's modulus *vs.* tensile strength *vs.* electrical conductivity for PANI containing free standing composites. Grey bars represent data obtained from the literature (Table S6, ESI†).

%, and a toughness of 770 ± 270 kJ/m^3. PANI/BANF/CNT demonstrated a Young's modulus of 4.0 ± 0.5 GPa, tensile strength of 40.0 ± 4.0 MPa, strain of 1.7 ± 0.2 %, and toughness of 430 ± 40 kJ/m^3. This can be attributed to the combined effect of the dilution of the BANFs, the strong interactions between PANI and BANFs, and the high rigidity of the PANI molecules.[6, 37] The rigid PANI molecules interact with the BANFs and SWCNTs through hydrogen bonding and π-π stacking interactions. More specifically, the PANI amine groups hydrogen-bond with the BANF amide groups, while PANI interacts with the BANF aromatic groups and the SWCNT sp^2-hybridized carbon atoms through π-π stacking interactions.[38, 59] The extensive hydrogen bonding and π-π stacking interactions facilitate load transfer within the BANF composites.[60]

The electrical conductivity of the composite films was measured using the four-point probe method, as shown in Fig. 3d and Table S5, ESI†. PANI/BANF composites demonstrated the lowest conductivity ($1.14 \cdot 10^{-3}$ ± $0.1 \cdot 10^{-3}$ S/cm) due to poor percolation. Electrical conductivity increased to 2.5 ± 0.4 S/cm upon addition of SWCNTs (PANI/BANF/CNT). Overall, the PANI/BANF/CNT composites exhibited the second highest conductivity despite the high BANF (73 wt%) content. BANF/CNT films demonstrated conductivity values of 0.13 ± 0.02 S/cm while PANI/CNT exhibited the highest conductivity with a value of 28 ± 1.4 S/cm. These results underline the significance of SWCNTs in the composites as they serve to create an electrically conductive network, assuring good electrical connectivity between PANI and BANF.[61]

Furthermore, the effect of SWCNT content in the PANI/BANF/CNT electrodes on the electrical and mechanical performance was investigated (Table S5, ESI†). The PANI content was kept constant (~15 wt%) while the BANF/CNT ratio varied from ~ 11 (7 wt% SWCNT) to ~ 2 (29 wt% SWCNT). Upon decreasing the BANF/CNT ratio from ~11 to ~ 6, electrical conductivity increased from 0.21 ± 0.03 S/cm to 2.5 ± 0.4 S/cm. Further decrease in the BANF/CNT ratio (from ~ 6 to ~ 2) did not lead to significant changes in electrical conductivity, indicating that percolation had already been achieved. In contrast, mechanical performance drastically deteriorated at lower BANF/CNT ratios. BANF/CNT ratios of ~11 (7 wt% SWCNT) led to a tensile strength of 48 ± 4.5 MPa, strain of 1.8 ± 0.2 %, Young's modulus of 4.6 ± 0.4 GPa, and toughness of 508 ± 20 kJ/m^3. Decreasing the BANF/CNT ratio to ~ 2 (29 wt% SWCNT) led to a tensile strength of 10.8 ± 1.7 MPa, strain of 1.2 ± 0.2 %, a Young's modulus of 1.4 ± 0.2 GPa, and a toughness of 81 ± 20 kJ/m^3. These results show that BANFs are critical to maintaining good mechanical properties in the composite electrodes. PANI/BANF/CNT electrodes containing 12 wt% CNT were selected for further electrochemical testing as they led to the best combination of mechanical and electrical properties.

Comparisons against other PANI-containing free-standing composites in the literature are shown in Fig. 3e and Table S6, ESI†. To date, only a handful of reports focus on free-standing PANI films due to PANI's low mechanical performance.[22] Herein, the composite electrodes were compared against two-layer PANI/ANF, PANI/polycarbonate (PC), PANI/bacterial cellulose (BC), PANI/chitosan (CS), PANI/ANF fabricated using vacuum filtration (VF), and PANI/CNT.[6, 24, 25, 37, 39, 62] All composites contained similar amounts of PANI (10 - 15 wt%). Our PANI/BANF/CNT composites exhibited a good combination of electrical and mechanical properties in the comparison. Two-layer PANI/ANF exhibited the highest reported electrical

conductivity (19.3 S/cm) and tensile strength (150 MPa) with a Young's modulus of 3.4 MPa.[37] The premade ANF layer served as the structural support while the impregnated layer of PANI ensured good electrical conductivity.[37] PANI/CS and PANI/CNT were fabricated by directly mixing PANI with CS and CNTs, respectively, leading to inhomogeneous films and as a result to an inferior mechanical performance.[24, 62] PANI/BC, PANI/PC, and PANI/ANF VF were prepared by polymerizing aniline in the presence of the other components, similar to our approach.[6, 25, 39] PANI/PC and PANI/ANF VF demonstrated relatively high tensile strengths but the electrical conductivities and Young's moduli were significantly inferior to the PANI/BANF/CNT composites.[6, 39] PANI/BC exhibited higher mechanical properties but with a lower electrical conductivity.[25] This comparison shows that the superior electrical conductivity of our PANI/BANF/CNT composites results from the continuous SWCNT conductive networks whereas the enhanced mechanical performance results from the extensive hydrogen bonding and π-π stacking interactions between BANFs, PANI, and SWCNTs. The good mechanical and electrical properties of the PANI/BANF/CNT make them ideal candidates for structural electrodes.

The electrochemical performance of the composite electrodes was evaluated in a two-electrode symmetric coin cell configuration using 6 M KOH aqueous electrolyte. More specifically, cyclic voltammetry (CV) was performed for PANI/CNT, PANI/BANF, PANI/BANF/12 wt% CNT, and BANF/CNT at 1 mV/s, as shown in Fig. 4a. The shapes of the CV curves for the PANI-containing electrodes indicate a pseudo-capacitive behaviour resulting from the redox-active nature of PANI.[63] leucoemeraldine/emeraldine and emeraldine/pernigraniline transitions of PANI.[61, 64]

The specific capacitance (based on active mass) for all electrodes was calculated at varying scan rates (1 – 100 mV/s) (Fig. 4b and Table S7, ESI†). BANF/CNT and PANI/BANF exhibited an inferior performance attributed to the low electrical conductivity and low content of the electrochemically active materials. PANI/CNT exhibited the highest specific capacitance values, with a specific capacitance of 299.1 ± 1.2 F/g at 1 mV/s. PANI/BANF/12 wt% CNT electrodes showed a similar behaviour despite the high content of BANFs (73 wt%), with a specific capacitance of 245.4 ± 2.6 F/g at 1 mV/s. CNTs and PANI form together a network that allows for fast electron and ion transport with increased surface area, facilitating fast redox reactions.[65] Specific capacitance decreased with scan rate for all electrodes resulting from diffusion limitations, as expected.[61,66]

Furthermore, galvanostatic cycling was conducted at 0.5 A/g. The curves exhibited quasi-triangular shapes resulting from the pseudocapacitive nature of PANI and the double-layer behaviour of CNTs, as shown in Fig. 4c. Prolonged galvanostatic cycling experiments were conducted up to 1,000 cycles (Fig. 4d and Table S8, ESI†). PANI/BANF and BANF/CNT electrodes did not reach 1,000 cycles due to their poor performance. The results are in agreement with the cyclic voltammetry tests. PANI/CNT and PANI/BANF/12 wt% CNT exhibited capacitance retentions of ~90 % and ~60 %, respectively. The lower capacitance retention of the BANF containing electrodes may be attributed to possible structural changes during cycling resulting from the swelling of BANFs in the electrolyte, as

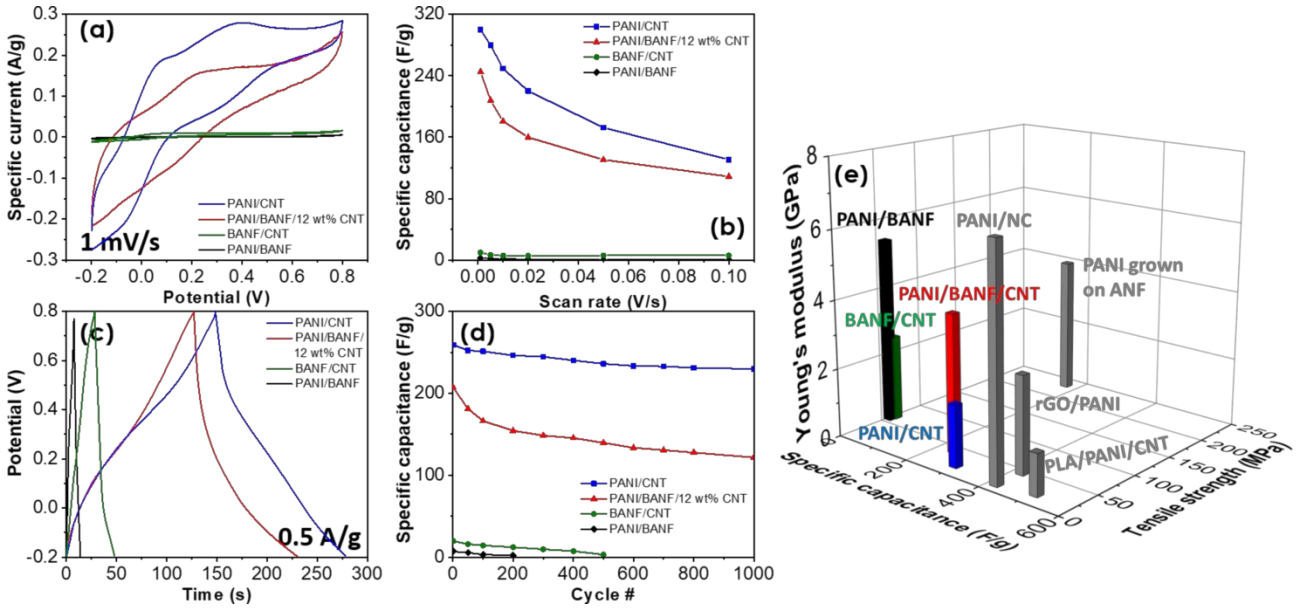

Fig. 4 (a) Cyclic voltammograms at 1 mV/s and (b) specific capacitance *vs.* scan rate for PANI/BANF, BANF/CNT, PANI/ BANF/12 wt% CNT, and PANI/CNT. (c) Galvanostatic charge-discharge curves and (d) specific capacitance *vs.* cycle number for all electrodes at 0.5 A/g. (e) Ashby plot of Young's modulus *vs.* specific capacitance *vs.* tensile strength for PANI-containing free-standing supercapacitor electrodes, see Table S9, ESI†. Specific capacitance values were calculated per active mass (PANI, CNT, and rGO mass).

PANI/CNT and PANI/BANF/12 wt% CNT exhibited two broad pairs of redox peaks attributed to the observed before in the literature.[67] Swelling of BANFs may close open pores, preventing the electrolyte penetration, and as a result leading to reduced cycling stability.

Finally, the structural supercapacitor electrodes were compared against other PANI containing free-standing electrodes from the literature, as shown in Fig. 4e, Fig. S3 and Table S9, ESI†. More specifically, PANI/BANF/12 wt% CNT electrodes were compared against rGO/PANI, polylactic acid (PLA)/CNT/PANI, PANI/nanocellulose (NC), and PANI grown on ANF.[20, 21, 40, 68] rGO/PANI, PLA/CNT/PANI, and PANI/NC exhibited higher specific capacitance values.[21, 68, 69] The enhanced energy storage performance of the rGO/PANI electrodes can be attributed to the higher PANI content (25.4 wt%).[69] The exact PANI content of the PANI/NC and PLA/CNT/PANI electrodes was not reported.[15, 21] Our PANI/BANF/12 wt% CNT electrodes exhibited a better combination of high energy storage, Young's modulus, and tensile strength. The better mechanical performance (tensile strength and Young's modulus) of the PANI/BANF/12 wt% CNT electrodes results from the strong BANFs and the extensive interfacial interactions (hydrogen bonding and π-π stacking interactions) within the composites. An Ashby plot based-on total electrode mass is shown in Fig. S3, ESI†. The PANI/BANF/12 wt% CNT electrodes exhibited a good combination of mechanical properties with a decent electrochemical performance in two electrode symmetric cells. At this point, it is worth mentioning the recent report on PANI grown on ANF premade films.[40] These electrodes exhibited a high tensile strength (233.3 MPa) with a similar Young's modulus (~4 GPa) to our electrodes, resulting from the strong premade ANF films/substrates.[40] The reported specific capacitance values in a two-electrode symmetric solid state device (~168 F/g based on active mass and 138 F/g based on total electrode mass) are comparable to our PANI/BANF/12 wt% CNT electrodes.[40] However, it is not possible to draw any further concrete conclusions regarding the energy storage performance (*i.e.* rate capability and cycling stability) as different testing configurations were used.

Besides being redox-active in aqueous media, as demonstrated above, PANI may also be utilized as the cathode in a non-aqueous Li-ion battery.[70] Towards this idea, the performance of a PANI/BANF/12 wt% CNT cathode in a Li-ion battery was investigated in a lithium metal half-cell. Specifically, Li metal foil was the anode and 1 M $LiPF_6$ in EC:DEC:DMC (1:1:1 v/v) was the electrolyte. Cyclic voltammetry was conducted at a scan rate of 1 mV/s in a 1.5 to 4 V *vs.* Li/Li^+ voltage range, as shown in Fig. 5a. The PANI/BANF/12 wt% CNT cell exhibited one pair of wide peaks due to the leucoemeraldine/emeraldine transformation,[18, 10, 65] whereas BANF/CNT showed no peaks. Capacitive plateaus are attributed to the CNTs.[71] Cyclic voltammograms at varying scan rates (1-100 mV/s) are shown in Fig. S4, ESI†. At higher scan rates the peaks disappear due to diffusion limitations.[72]

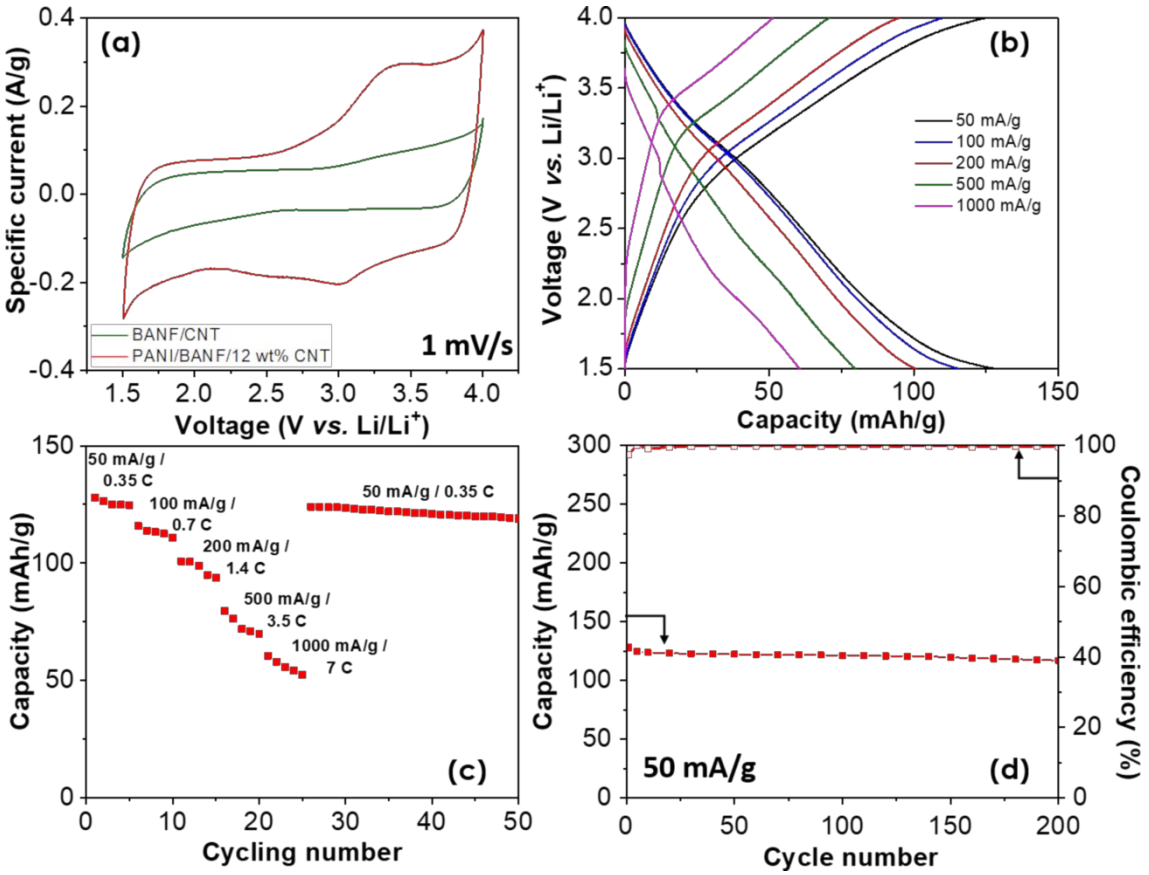

Fig. 5 (a) Cyclic voltammograms at 1 mV/s for BANF/CNT (green) and PANI/BANF/12 wt% CNT (red) electrodes in a lithium metal half-cell. (b) Galvanostatic charge-discharge curves at varying specific currents (50 – 1000 mA/g), (c) rate capability, and (d) prolonged galvanostatic cycling at 50 mA/g for 200 cycles for a PANI/BANF/12 wt% CNT cathode. Capacity was calculated based on the mass of PANI.

Fig. 5b and 5c presents the charge-discharge voltage profiles at varying specific currents (50 – 1000 mA/g) and the rate

capability, respectively. The discharge capacity at 50 mA/g was 128 mAh/g, whereas at 1000 mA/g the discharge capacity dropped to 61 mAh/g. Subsequently, a capacity of 124 mAh/g was recovered at 50 mA/g, indicating the high stability of the electrodes. Prolonged charge-discharge tests at 50 mA/g were conducted for 200 cycles, Fig. 5d and Fig. S5. After 200 cycles, the discharge capacity was maintained at 116 mAh/g with a coulombic efficiency of 99.1 % (*vs.* 97 % for the first cycle). The obtained capacity values are comparable with the theoretical capacity of PANI (147 mAh/g for one electron transferred per two repeat units), underlining the exceptional energy storage performance of the PANI/BANF/12 wt% CNT cathodes.

Furthermore, we conducted electrochemical impedance spectroscopy (EIS) before and after 25 cycles at 3.3 V *vs.* Li/Li$^+$. Fig. S6 shows the Nyquist plot, while the inset shows the equivalent circuit used to analyse the EIS data. The Nyquist plots before and after cycling exhibited a similar behaviour, with one semicircle at high frequency and a long diffusive tail at low frequency. In the equivalent circuit, R_S (intercept with the real axis) is attributed to the electrolyte resistance, R_{CT} represents the charge transfer impedance, *CPE* represents the non-ideal electric double layer capacitance, and W_o represents the Warburg impedance due to the lithium ion diffusion in the bulk of the electrode.[73] Before cycling the fitted value of R_{CT} was 25 Ω and after 25 cycles R_{CT} decreased to 12 Ω. The angle of the diffusive tail which is indicative of lithium ion diffusion[74] decreased slightly from 74° to 66°. The low R_{CT} values[75] and the relatively small variation in the EIS data with cycling indicate the good electronic conductivity and structural stability of the PANI/BANF/12 wt% CNT cathodes. The good structural stability was further demonstrated using SEM on PANI/BANF/12 wt% CNT cathodes after 200 cycles (Fig. S7), where no significant structural changes were observed.

Ragone plots of specific power *vs.* specific energy and power density *vs.* energy density are shown in Fig. S8, ESI†. The PANI/BANF/CNT electrodes exhibited a maximum specific energy value of 320 mWh/g at a specific power of 8,000 mW/g, and a maximum specific power of 9,166 mW/g at a specific energy of 138 mWh/g. Similarly, the highest energy density was 243 mWh/L at a power density of 11,550 mW/L and the maximum power density was 13,250 mW/L at an energy density of 105 mWh/L.

Table S10, ESI† shows a comparison of our electrodes against other PANI-based battery electrodes such as PANI/MXene, PANI/rGO, PANI/SWCNTs aerogels, PANI/MWCNTs, and PANI/polyoxometalate.[11, 18, 76-78] Despite the low PANI content (~15 wt%), the PANI/BANF/12 wt% CNT electrodes exhibited comparable but lower capacities as compared to the literature. However, notably, our electrodes were free-standing with good mechanical properties, whereas the mechanical properties were not reported for these prior reports. Further, most of the prior electrodes were coated onto conductive substrates for structural support.[11, 18, 77, 78] This comparison demonstrates that the PANI/BANF/12 wt% CNT electrodes are potential candidates for structural cathode materials in Li-ion batteries due to their high capacity, good rate charge-discharge performance, good cycle performance, and mechanical performance.

To further investigate the charge storage mechanism of the PANI/BANF/12 wt% CNT cathodes in the Li-ion battery environment, the Faradaic and non-Faradaic contributions were distinguished using equation 1:

$$i = a \cdot v^b \quad (1)$$

where i is the specific current (A/g), v the scan rate (mV/s), and a and b are adjustable parameters.[18, 79, 80] The redox process is considered as an ideal Faradaic process when b is 0.5, whereas when b is 1 the process is considered to be a non-Faradaic process. Values between 0.5 and 1 indicate a mixed mechanism.[11, 16, 18, 80] The b-values for the PANI/BANF/12 wt% CNT cathodes were obtained from the slope of the log (i) *vs.* log (v) graphs for scan rates of 1 – 20 mV/s, as shown in Fig. S9, ESI†. Fig. S9c, ESI† shows the b-values obtained from the anodic and cathodic scans from 1.5 to 4 V. More specifically, in the cathodic scans, the b-value reached a minimum of b = 0.47 at 3 V, which is in accordance with the Faradaic peak observed in the CV curves. Similarly, in the anodic scans the b-value reached a minimum of b = 0.46 at 3.3 V. The results indicate qualitatively that charge storage within the PANI/BANF/12 wt% CNT electrodes occurred with mixed Faradaic (due to PANI's

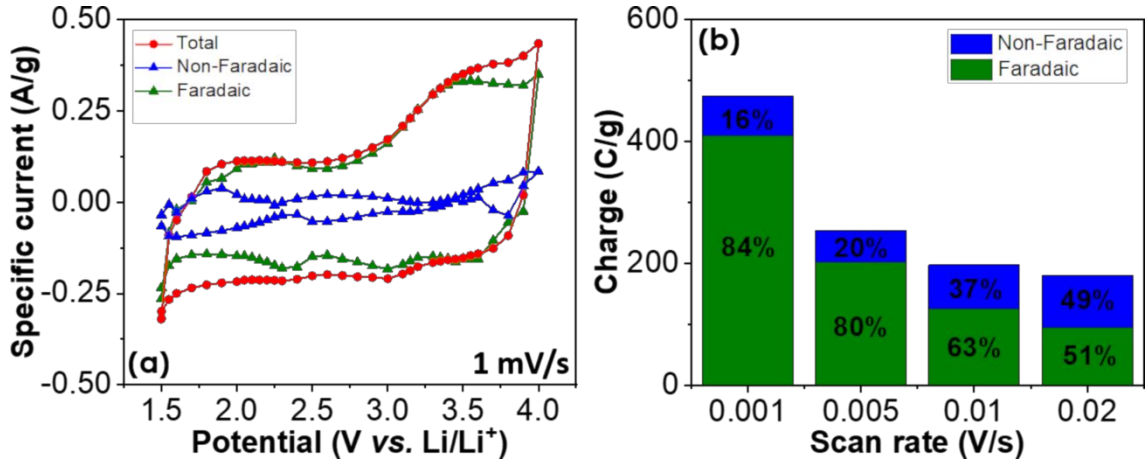

Fig. 6 Cyclic voltammetry (a) at 1 mV/s for PANI/BANF/12 wt% CNT cathodes and (b) charge stored at different scan rates displaying the Faradaic (green) and non-Faradaic (blue) contribution.

leucoemeraldine/emeraldine transformation) and non-Faradaic contributions.

Additionally, the relative contributions of Faradaic and non-Faradaic charge storage were calculated using equation 2:

$$i = a_1 \cdot v + a_2 \cdot v^{0.5} \quad (2)$$

where i is the specific current (A/g) and a_1 and a_2 are the relative contributions of the non-Faradaic and Faradaic processes, respectively.[11, 18, 73] The values of a_1 and a_2 were obtained from the slopes and intercepts of the $i/v^{0.5}$ *vs.* $v^{0.5}$ plots (Fig. S10, ESI†). From this analysis, we reconstructed the cyclic voltammetry plot at 1 mV/s, as shown in Fig. 6a. The blue line corresponds to the non-Faradaic processes, the green to the Faradaic, and the red to the total specific current. The results indicate that the charge storage mechanism is dominated by Faradaic processes. Fig. 6b shows the percentage contributions of non-Faradaic and Faradaic mechanisms at various scan rates (1 mV/s – 20 mV/s). The Faradaic charge storage decreased from 84 % to 51 % with scan rate, which is typical for PANI-based electrodes due to diffusion limitations.[11]

Conclusions

Structural electrodes for supercapacitors and batteries based on PANI, BANFs, and CNTs were developed. BANFs served as the load bearing component while CNTs and PANI facilitated fast electronic transport. Further, PANI stored charge through its conversion among leucoemeraldine, emeraldine, and pernigraniline states. Extensive hydrogen bonding and π-π stacking interactions within the composite electrodes were harnessed, leading to high mechanical performance (tensile strength and Young's modulus). The continuous networks created by BANFs, CNTs, and PANI led to a good combination of energy storage and mechanical performance as compared to the literature, making them ideal candidates for structural electrodes. The structural electrodes exhibited capacity values (128 ± 5 mAh/g) comparable to the theoretical capacity of PANI (147 mAh/g), indicating the PANI was nearly fully utilized. The charge storage mechanism was further investigated by distinguishing the Faradaic and non-Faradaic contributions. As expected for PANI-based electrodes mixed contributions were obtained. This work demonstrates an efficient route for designing and fabricating structural electrodes with high energy storage performance.

Conflicts of interest

There are no conflicts to declare.

Acknowledgements

The authors acknowledge the TAMU Materials Characterization Facility. J.L.L. acknowledges the William and Ruth Neely Faculty Fellowship. This work was supported by Air Force Office of Scientific Research Grant No. FA9550-19-1-0170.

References

1. W. Liu, M.-S. Song, B. Kong and Y. Cui, *Adv. Mater.*, 2017, **29**, 1603436.
2. K. Jost, G. Dion and Y. Gogotsi, *Journal of Materials Chemistry A*, 2014, **2**, 10776-10787.
3. S. R. Kwon, J. Harris, T. Zhou, D. Loufakis, J. G. Boyd and J. L. Lutkenhaus, *ACS Nano*, 2017, **11**, 6682-6690.
4. F. Fusalba, P. Gouérec, D. Villers and D. Bélanger, *J. Electrochem. Soc.*, 2001, **148**, A1-A6.
5. Y.-Z. Long, M.-M. Li, C. Gu, M. Wan, J.-L. Duvail, Z. Liu and Z. Fan, *Prog. Polym. Sci.*, 2011, **36**, 1415-1442.
6. B. H. Jeon, S. Kim, M. H. Choi and I. J. Chung, *Synthetic Metals*, 1999, **104**, 95-100.
7. J.-W. Jeon, S. R. Kwon, F. Li and J. L. Lutkenhaus, *ACS Applied Materials & Interfaces*, 2015, **7**, 24150-24158.
8. J.-W. Jeon, J. O'Neal, L. Shao and J. L. Lutkenhaus, *ACS Applied Materials & Interfaces*, 2013, **5**, 10127-10136.
9. A. G. MacDiarmid and A. J. Epstein, *Synth. Met.*, 1994, **65**, 103-116.
10. A. G. MacDiarmid, L. S. Yang, W. S. Huang and B. D. Humphrey, *Synth. Met.*, 1987, **18**, 393-398.
11. J. Yun, I. Echols, P. Flouda, S. Wang, A. Easley, X. Zhao, Z. Tan, E. Prehn, G. Zi, M. Radovic, M. J. Green and J. L. Lutkenhaus, *ACS Applied Materials & Interfaces*, 2019, DOI: 10.1021/acsami.9b16692.
12. H. R. Ghenaatian, M. F. Mousavi and M. S. Rahmanifar, *Electrochim. Acta*, 2012, **78**, 212-222.
13. S. R. Kwon, J.-W. Jeon and J. L. Lutkenhaus, *RSC Advances*, 2015, **5**, 14994-15001.
14. Q. Wu, Y. Xu, Z. Yao, A. Liu and G. Shi, *ACS Nano*, 2010, **4**, 1963-1970.
15. C. Meng, C. Liu and S. Fan, *Electrochem. Commun.*, 2009, **11**, 186-189.
16. L. Shao, J.-W. Jeon and J. L. Lutkenhaus, *Journal of Materials Chemistry A*, 2014, **2**, 14421-14428.
17. S. Moon, Y. H. Jung and D. K. Kim, *J. Power Sources*, 2015, **294**, 386-392.
18. J.-W. Jeon, S. R. Kwon and J. L. Lutkenhaus, *Journal of Materials Chemistry A*, 2015, **3**, 3757-3767.
19. M. Yanilmaz, M. Dirican, A. M. Asiri and X. Zhang, *Journal of Energy Storage*, 2019, **24**, 100766.
20. H. H. Hsu, A. Khosrozadeh, B. Li, G. Luo, M. Xing and W. Zhong, *ACS Sustainable Chemistry & Engineering*, 2019, **7**, 4766-4776.
21. Q. Wang, H. Wang, P. Du, J. Liu, D. Liu and P. Liu, *Electrochimica Acta*, 2019, **294**, 312-324.
22. H. Valentová and J. Stejskal, *Synth. Met.*, 2010, **160**, 832-834.
23. V. Mottaghitalab, G. M. Spinks and G. G. Wallace, *Synth. Met.*, 2005, **152**, 77-80.
24. F. M. Blighe, D. Diamond, J. N. Coleman and E. Lahiff, *Carbon*, 2012, **50**, 1447-1454.
25. W. Hu, S. Chen, Z. Yang, L. Liu and H. Wang, *The Journal of Physical Chemistry B*, 2011, **115**, 8453-8457.
26. S. R. Kwon, M. B. Elinski, J. D. Batteas and J. L. Lutkenhaus, *ACS Appl Mater Interfaces*, 2017, **9**, 17125-17135.
27. P. Flouda, X. Y. Feng, J. G. Boyd, E. L. Thomas, D. C. Lagoudas and J. L. Lutkenhaus, *Batteries & Supercaps*, 2019, **2**, 464-472.

28. P. Flouda, S. A. Shah, D. C. Lagoudas, M. J. Green and J. L. Lutkenhaus, *Matter*, 2019, **1**, 1532-1546.
29. W. Sun, S. A. Shah, J. L. Lowery, J. H. Oh, J. L. Lutkenhaus and M. J. Green, *Advanced Materials Interfaces*, **0**, 1900786.
30. S. A. Shah, D. Kulhanek, W. Sun, X. Zhao, S. Yu, D. Parviz, J. L. Lutkenhaus and M. J. Green, *J. Colloid Interface Sci.*, 2019, DOI: https://doi.org/10.1016/j.jcis.2019.10.066.
31. A. G. Patel, L. Johnson, R. Arroyave and J. L. Lutkenhaus, *Mol Syst Des Eng*, 2019, **4**, 654-663.
32. P. Flouda, J. Yun, D. Loufakis, S. A. Shah, M. J. Green, D. C. Lagoudas and J. L. Lutkenhaus, *Sustainable Energy & Fuels*, 2020, **4**, 2301-2308.
33. L. Xu, X. Zhao, C. Xu and N. A. Kotov, *Adv. Mater*, 2018, **30**, 1703343-n/a.
34. M. Yang, K. Cao, L. Sui, Y. Qi, J. Zhu, A. Waas, E. M. Arruda, J. Kieffer, M. D. Thouless and N. A. Kotov, *ACS Nano*, 2011, **5**, 6945-6954.
35. J. Zhu, M. Yang, A. Emre, J. H. Bahng, L. Xu, J. Yeom, B. Yeom, Y. Kim, K. Johnson, P. Green and N. A. Kotov, *Angew. Chem. Int. Ed.*, 2017, **56**, 11744-11748.
36. M. Yang, K. Q. Cao, B. Yeom, M. D. Thouless, A. Waas, E. M. Arruda and N. A. Kotov, *J. Compos. Mater.*, 2015, **49**, 1873-1879.
37. J. Lyu, X. Zhao, X. Hou, Y. Zhang, T. Li and Y. Yan, *Compos. Sci. Technol.*, 2017, **149**, 159-165.
38. Y. Zhao, S. Zhang, F. Hu, J. Li, H. Chen, J. Lin, B. Yan, Y. Gu and S. Chen, *Journal of Materials Science: Materials in Electronics*, 2019, **30**, 12718-12728.
39. X. Han, L. Lv, D. Yu, X. Wu and C. Li, *ACS Applied Materials & Interfaces*, 2019, **11**, 3466-3473.
40. Q. Yin, H. Jia, A. Mohamed, Q. Ji and L. Hong, *Nanoscale*, 2020, **12**, 5507-5520.
41. J. Zhu, M. Yang, A. Emre, J. H. Bahng, L. Xu, J. Yeom, B. Yeom, Y. Kim, K. Johnson, P. Green and N. A. Kotov, *Angewandte Chemie*, 2017, **129**, 11906-11910.
42. A. Eftekhari, L. Li and Y. Yang, *Journal of Power Sources*, 2017, **347**, 86-107.
43. L. L. Zhang and X. S. Zhao, *Chemical Society Reviews*, 2009, **38**, 2520-2531.
44. Y. J. Kim, T. S. Shin, H. D. Choi, J. H. Kwon, Y.-C. Chung and H. G. Yoon, *Carbon*, 2005, **43**, 23-30.
45. B. Marinho, M. Ghislandi, E. Tkalya, C. E. Koning and G. de With, *Powder Technology*, 2012, **221**, 351-358.
46. H. Wang, S. Lu, Y. Chen, L. Han, J. Zhou, X. Wu and W. Qin, *Journal of Materials Chemistry A*, 2015, **3**, 23677-23683.
47. Y. Cheng, S. Lu, H. Zhang, C. V. Varanasi and J. Liu, *Nano Letters*, 2012, **12**, 4206-4211.
48. J. Y. Kim and Y. J. Park, *Scientific Reports*, 2017, **7**, 8610.
49. L. Penn and F. Milanovich, *Polymer*, 1979, **20**, 31-36.
50. E. N. Konyushenko, J. Stejskal, M. Trchová, J. Hradil, J. Kovářová, J. Prokeš, M. Cieslar, J.-Y. Hwang, K.-H. Chen and I. Sapurina, *Polymer*, 2006, **47**, 5715-5723.
51. S. Y. Kim, J. Hong, R. Kavian, S. W. Lee, M. N. Hyder, Y. Shao-Horn and P. T. Hammond, *Energ Environ Sci*, 2013, **6**, 888-897.
52. S. He, J. Wei, F. Guo, R. Xu, C. Li, X. Cui, H. Zhu, K. Wang and D. Wu, *Journal of Materials Chemistry A*, 2014, **2**, 5898-5902.
53. G. Xiao, J. Di, H. Li and J. Wang, *Composites Science and Technology*, 2020, **189**, 108021.
54. B. Yang, X. Ding, M. Zhang, L. Wang and X. Huang, *Composites Communications*, 2020, **17**, 192-196.
55. F. Xie, F. Jia, L. Zhuo, Z. Lu, L. Si, J. Huang, M. Zhang and Q. Ma, *Nanoscale*, 2019, **11**, 23382-23391.
56. J. Luo, M. Zhang, J. Nie, G. Liu, J. Tan, B. Yang, S. Song and J. R. Zhao, *Polymer Degradation and Stability*, 2019, **167**, 170-178.
57. B. Yang, L. Wang, M. Zhang, J. Luo and X. Ding, *ACS Nano*, 2019, **13**, 7886-7897.
58. F. Wang, Y. Wu, Y. Huang and L. Liu, *Composites Science and Technology*, 2018, **156**, 269-275.
59. Q. Yao, L. Chen, W. Zhang, S. Liufu and X. Chen, *ACS Nano*, 2010, **4**, 2445-2451.
60. Y. Guan, W. Li, Y. L. Zhang, Z. Q. Shi, J. Tan, F. Wang and Y. H. Wang, *Composites Science and Technology*, 2017, **144**, 193-201.
61. F. Liu, S. Luo, D. Liu, W. Chen, Y. Huang, L. Dong and L. Wang, *ACS Applied Materials & Interfaces*, 2017, **9**, 33791-33801.
62. T. Thanpitcha, A. Sirivat, A. M. Jamieson and R. Rujiravanit, *Carbohydr. Polym.*, 2006, **64**, 560-568.
63. P. Simon, Y. Gogotsi and B. Dunn, *Science*, 2014, **343**, 1210-1211.
64. F. Miao, C. Shao, X. Li, K. Wang, N. Lu and Y. Liu, *ACS Sustainable Chemistry & Engineering*, 2016, **4**, 1689-1696.
65. P. Liu, J.-J. Han, L.-F. Jiang, Z.-Y. Li and J.-N. Cheng, *Appl. Surf. Sci.*, 2017, **400**, 446-452.
66. J.-S. M. Lee, M. E. Briggs, C.-C. Hu and A. I. Cooper, *Nano Energy*, 2018, **46**, 277-289.
67. A. Patel, K. Wilcox, Z. Li, I. George, R. Juneja, C. T. Lollar, S. Lazar, J. C. Grunlan, W. E. Tenhaeff and J. L. Lutkenhaus, *ACS Applied Materials & Interfaces*, 2020, DOI: 10.1021/acsami.0c03671.
68. W. Zheng, R. Lv, B. Na, H. Liu, T. Jin and D. Yuan, *Journal of Materials Chemistry A*, 2017, **5**, 12969-12976.
69. R. Hu, J. Zhao, G. Zhu and J. Zheng, *Electrochimica Acta*, 2018, **261**, 151-159.
70. P. Novák, K. Müller, K. S. V. Santhanam and O. Haas, *Chemical Reviews*, 1997, **97**, 207-282.
71. M. N. Hyder, S. W. Lee, F. Ç. Cebeci, D. J. Schmidt, Y. Shao-Horn and P. T. Hammond, *ACS Nano*, 2011, **5**, 8552-8561.
72. W.-M. Chen, L. Qie, L.-X. Yuan, S.-A. Xia, X.-L. Hu, W.-X. Zhang and Y.-H. Huang, *Electrochim. Acta*, 2011, **56**, 2689-2695.
73. K. T. Sarang, A. Miranda, H. An, E.-S. Oh, R. Verduzco and J. L. Lutkenhaus, *ACS Applied Polymer Materials*, 2019, **1**, 1155-1164.
74. H. An, X. Li, C. Chalker, M. Stracke, R. Verduzco and J. L. Lutkenhaus, *ACS Applied Materials & Interfaces*, 2016, **8**, 28585-28591.
75. L. Yang, S. Wang, J. Mao, J. Deng, Q. Gao, Y. Tang and O. G. Schmidt, *Advanced Materials*, 2013, **25**, 1180-1184.
76. D. Ge, L. Yang, A. Honglawan, J. Li and S. Yang, *Chemistry of Materials*, 2014, **26**, 1678-1685.
77. B.-L. He, B. Dong, W. Wang and H.-L. Li, *Materials Chemistry and Physics*, 2009, **114**, 371-375.
78. H. Yang, T. Song, L. Liu, A. Devadoss, F. Xia, H. Han, H. Park, W. Sigmund, K. Kwon and U. Paik, *The Journal of Physical Chemistry C*, 2013, **117**, 17376-17381.
79. L. Shao, J.-W. Jeon and J. L. Lutkenhaus, *Journal of Materials Chemistry A*, 2013, **1**, 7648-7656.

80. H. Lindström, S. Södergren, A. Solbrand, H. Rensmo, J. Hjelm, A. Hagfeldt and S.-E. Lindquist, *The Journal of Physical Chemistry B*, 1997, **101**, 7717-7722.

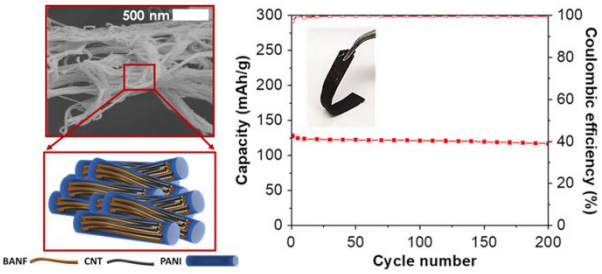

Continuous networks of branched aramid nanofibers, polyaniline, and carbon nanotubes led to mechanically enhanced supercapacitor and battery electrodes.